ELSEVIER

Contents lists available at ScienceDirect

Materials Today Communications

journal homepage: www.elsevier.com/locate/mtcomm





Advanced dual-responsive silicone-based nanocomposites: Enhancing the de-icing efficacy of power transmission lines by harnessing magnetic and solar energy

Shamim Roshan ^{a,*}, Gelareh Momen ^{a,b}, Reza Jafari ^a, Issouf Fofana ^a, Stephan Brettschneider ^a

ARTICLE INFO

Keywords: Silicone-based nanocomposites Anti-icing coating De-icing properties Photothermal characteristics Thermomagnetic properties Fe₃O₄ nanoparticles

ABSTRACT

In regions prone to severe weather, ice accumulation on power transmission lines creates significant challenges, including structural damage and power outages. Although various de-icing strategies exist, many are laborintensive, costly, and provide only short-term solutions. This study introduces a novel nanocomposite coating composed of surface-modified iron oxide nanoparticles embedded in a silicone-based polymer. This coating harnesses thermomagnetic and photothermal properties to convert magnetic and solar energy into heat to produce effective de-icing of transmission lines. We evaluated the surface characteristics using contact and sliding angle measurements, profilometry, and differential scanning calorimetry, along with freezing delay and ice adhesion tests under nonimpact conditions. The 30 wt% nanoparticle coating achieved the highest contact angle (116°), whereas the 20 wt% coating (SFe20) demonstrated superior performance with the lowest sliding angle (12° \pm 0.8°) and ice nucleation temperature (-25.1 °C). Under simulated sunlight, the SFe20 coating melted ice within 210 s, raising the surface temperature from -5 °C to 21 °C. Additionally, its thermomagnetic response facilitated ice detachment at low temperatures, with surface temperature changes twice that of the control samples lacking nanoparticles. These findings demonstrate that the SFe20 coating is a promising, energy-efficient alternative to conventional mechanical and thermal de-icing methods in the power industry.

1. Introduction

Icing on power transmission lines poses a critical challenge in colder regions, such as Canada, the UK, China, Norway, and the US. This ice accumulation can lead to severe damage, including line collapse and widespread outages, resulting in extensive maintenance, high repair costs, and frequent power interruptions [1–8]. Addressing icing is essential for maintaining the reliability and safety of power infrastructure in cold climates. Various strategies exist to mitigate ice accumulation on power lines, with mechanical removal being one of the most common. This method involves using specialized equipment or manual labor to physically clear ice from the lines [9]. However, mechanical ice removal is time-consuming and often inefficient, particularly over extensive networks. The process provides only temporary results, as ice and snow quickly reaccumulate in harsh weather. Additionally, the

de-icing equipment and infrastructure experience significant wear and tear, increasing maintenance costs and reducing their lifespans. Therefore, there is a pressing need for more durable, efficient, and cost-effective solutions to address icing challenges in the power industry [9–11].

One of the most effective strategies for preventing ice formation on power lines uses thermal methods to maintain conductor temperatures above freezing, notably through the Joule effect [12]. However, this method has significant drawbacks, including high operational costs and substantial energy consumption, which make it less feasible in terms of sustainability and long-term affordability.

Recently, new anti-icing and de-icing techniques have emerged, including superhydrophobic surfaces [13,14], slippery liquid-infused porous surfaces (SLIPS) [15,16], photothermal materials [17,18], electrothermal materials [19–21], and thermomagnetic materials [22].

E-mail address: sroshan@etu.uqac.ca (S. Roshan).

^a International Research Centre for Nordic Engineering (CIIN), Department of Applied Sciences, University of Québec in Chicoutimi (UQAC), 555, boul. de l'Université, Chicoutimi, Québec G7H 2B1, Canada

^b Département De Génie Aérospatial, ÉCole De Technologie Supérieure, 1100 Notre-Dame St W, Montreal, Quebec H3C 1K3, Canada

^{*} Corresponding author.

Evaluations of passive coatings on conductors and external insulators have revealed a notable market gap for products specifically tailored to conductors, highlighting the need for innovation in protective solutions. For active coating strategies, conventional methods, e.g., ice electrolysis or applying pulsed currents to conductive layers, have proven inefficient or impractical [22]. Nevertheless, active coatings, particularly ferromagnetic coatings, show promise by effectively melting wet snow on these structures. Photo/electrothermal materials and thermomagnetic coatings are common anti-icing solutions because of their low cost and long lifespan, although they can be sensitive to sunlight and the existing magnetic fields around electrical conductors [23,24].

Among active anti-icing approaches, electrothermal coatings based on carbon nanomaterials such as carbon nanotubes (CNTs) and graphene foams have attracted considerable attention due to their exceptionally high electrical conductivity, thermal stability, and three-dimensional conductive architectures, enabling rapid and uniform Joule heating [20,21]. These coatings can typically raise the surface temperature within seconds under low applied voltages, resulting in immediate melting of ice and snow [21].

Despite these advantages, the performance of such systems is inherently dependent on a direct electrical power supply, which can be costly and operationally challenging for large-scale applications such as power transmission lines in remote areas. In addition, installation of wiring and power-delivery systems on existing infrastructure is complex, and the continuous energy demand can lower overall system efficiency. Another critical limitation is the high cost of carbon nanomaterials (e.g., CNTs, graphene), which can hinder large-scale commercialization and limit their economic feasibility for widespread deployment [25].

These limitations have prompted growing interest in alternative approaches such as thermomagnetic coatings

Magnetic nanomaterials have emerged as promising candidates for use as heat mediators because of their ability to absorb energy from light and convert it to heat under specific conditions [26,27]. These materials are particularly effective when exposed to external alternating current (AC) magnetic fields, making them valuable for anti-icing applications where localized heating is necessary [28,29].

Magnetic nanocomposite materials have garnered significant interest for their unique physical properties, including electrical conductivity, sensitivity to magnetic fields, and excellent light-absorption capabilities [30,31]. Magnetic nanoparticles, particularly Fe_3O_4 (magnetite), are commonly embedded in a polymeric matrix to create nanocomposites that combine magnetic functionality with enhanced mechanical strength [32,33]. Iron oxide nanoparticles are known for their excellent magnetic properties and their ability to convert magnetic energy into thermal energy [23,24]. When embedded in a suitable polymeric matrix, these nanoparticles can uniformly absorb magnetic radiation and generate heat, effectively melting ice on the conductor's surface [34].

Several studies have highlighted the potential of iron oxide nanoparticles for heat generation in coatings. Yiqing et al. prepared a nanocomposite combining Fe₃O₄ nanoparticles and a polyetherimide (PEI) substrate. They created a superhydrophobic microstructure on the surface of the modified PEI using lithography. The coating's photothermal response could raise its temperature to 100 °C, melting frost on the surface [35]. Furthermore, Zhang et al [36]. demonstrated the feasibility of using magnetic nanoparticles for anti-icing and de-icing applications. They designed slippery polyol-infused porous surfaces (SPIPSs) using various polyols as the lubricating agents. These SPIPSs were produced using amino-modified magnetic Fe₃O₄ nanoparticles and amphiphilic copolymer hybrids that were covalently cross-linked. The active thermal de-icing capability of these slippery surfaces is derived from the inherent photothermal effects of magnetic Fe₃O₄ nanoparticles. Xiao et al [37]. used PDMS polymers to produce icephobic surfaces and found that nanoparticles embedded in these polymers not only prevented ice formation but also made ice removal easier and reduced surface adhesion. Cheng et al [38]. used up to 50 wt% of amino-functionalized magnetite particles dispersed in a fluorinated

copolymer modified with epoxy groups. The Fe $_3$ O₄ nanoparticles exhibited significant magnetic properties, efficiently converting magnetic energy to thermal energy under alternating magnetic fields.

Although these pioneering studies are promising, challenges persist, including high costs and performance issues under low-light conditions. Additionally, most solutions rely on synthesized materials or require multiple steps to achieve the final coating structure; moreover most studies focus solely on the photothermal responsiveness of Fe₃O₄ nanoparticles. To address these challenges and knowledge gaps, here we propose a one-step, low-cost, dual-responsive icephobic coating. Despite significant progress in developing icephobic coatings, no study, to our knowledge, has investigated the thermomagnetic properties of silicone-based nanocomposites at low temperatures, particularly in the context of in situ heat generation during the ice-melting process.

In this study, hybrid coatings based on a silicone-based polymeric coating were developed by incorporating iron oxide nanoparticles modified with silicone oil to enhance nanoparticle dispersion and improve icephobicity. This coating relies on both magnetic and solar energy absorption to achieve effective de-icing properties. The coating's wettability, surface roughness, ice nucleation temperature, and adhesion properties under cold conditions were systematically evaluated. Furthermore, the thermomagnetic and photothermal effects were explored to demonstrate the coating's potential for practical de-icing applications.

2. Materials and methods

Sheets of aluminum 2024-T3 (AA2024T3) were selected as the substrate and contained the following composition by weight: 4.1 % Cu, 1.5 % Mg, 0.7 % Mn, 0.5 % Fe, 0.3 % Zn, 0.15 % Ti, and 0.1 % Ni, with the balance being Al. The Sylgard®184 silicone elastomer kit was obtained from Dow Corning Corporation. n-hexane (99 %), serving as a solvent, was obtained from Thermo Fisher Scientific, and oil-treated Fe₃O₄ nanoparticles were purchased from US-Nano Co.

To fabricate the nanocomposites, we combined varying proportions of nanoparticles (10, 20, and 30 wt% relative to the weight of the resin and hardener) with n-hexane. This mixture was sonicated at 100 W for 10 min to ensure uniform dispersion of the Fe₃O₄ nanoparticles. The solvent-nanoparticle blend was then mixed with Sylgard® 184 resin and subjected to sonication at 100 W for 3 min, using an ice bath to maintain a low temperature. After sonication, the curing agent was added at a standard 1:10 ratio and stirred for 10 min. A vacuum was employed after the mixing process to eliminate any trapped air, ensuring a uniform and defect-free coating. The resulting mixtures, along with a reference mixture without nanoparticles, were applied to clean aluminum substrates using a spin coater (Zehntner ZUA2000 universal applicator). In order to achieve high thickness coatings, the spin coating speed and coating drop rate were 50 rpm during 0.2 mL/s respectively. The coated samples were cured in an oven at 120 °C for 3 h to obtain fully cured coatings. A schematic illustration of the coating fabrication process is shown in Fig. 1.

The samples were labeled according to their Fe $_3O_4$ nanoparticle content, SFex, where SFe refers to the silicon coatings containing Fe $_3O_4$ nanoparticles and x represents the nanoparticle content (i.e., 0, 10, 20, and 30 wt%). The mean dry thickness of the coatings was approximately $300\pm20~\mu m$, as measured using a DeFelsko PosiTector 200 and an Elektrophysik MiniTest70 coating thickness gauge. We examined the effect of Fe $_3O_4$ nanoparticles in the silicon coatings using an optical profilometer (Profilm3D Filmetrics®, USA) with white light interferometry (WLI), allowing surface profiles and roughness measurements down to 0.05 μm across a designated area of 250 by 200 μm . Three random locations were selected for evaluating each sample.

The surface structure and nanoparticle distribution in the nanocomposites were examined using field emission scanning electron microscopy (Leica Microsystems EM VCT500 Cryo-Transfer System) combined with energy-dispersive X-ray spectroscopy (EDX, EDAX

Fig. 1. Schematic of the fabrication of hybrid coatings.

Octane Ultra $100~\text{mm}^2$ SDD with TEAM 3D EDS Analysis System) to analyze the elemental composition of the microzones in the coatings.

Differential scanning calorimetry (DSC Q250, TA Instruments, New Castle, DE, USA) was used to determine the effect of the nanoparticle concentration on ice formation on the silicone-based coatings. We added 5 mg of water to a DSC pan, which was then coated with a thin layer of each sample and sealed with a lid; an empty pan served as the reference. The method included cooling from 40 to -40 °C at a rate of 5 °C·min⁻¹. A Kruss contact angle meter was used, maintaining the cooling chamber at -20 °C, to assess the impact of various Fe₃O₄ nanoparticle levels on freezing time delays. The adhesive strength of the ice on the test samples was evaluated using a push-off test conducted at -10 °C. A plastic mold measuring 1.2 cm in diameter was placed on the samples and filled with distilled water. After a 24 h freezing period, the probe moved toward the cylindrical column at a rate of 0.05 mm/s and applied a force until the frozen cylinder separated from the sample surface the force required to remove the ice was measured with a force gauge to assess ice adhesion. We evaluated the contact angle (CA) and sliding angle (SA) using a KrussTM DSA 100 goniometer under ambient and subzero conditions. In the static CA tests, a $4\,\mu L$ droplet of distilled water was placed on the coated surfaces, and the angle was measured through drop shape analysis using the Young-Laplace approximation method. The results are presented as the average (and standard deviation) of five random measurements from each sample surface.

To assess the photothermal characteristics of the developed coatings, free-standing films were prepared to eliminate the substrate effects on heat transfer. Before each evaluation, the samples were placed on a 3 cm thick cubic foam to minimize heat dissipation. They were then exposed to light from a xenon lamp, simulating natural sunlight at an intensity of around 1 kW/m², at room temperature with a wavelength range of 240–2400 cm⁻¹. The sample temperature was monitored using an Optris PIX infrared camera. To evaluate the de-icing capabilities of the coatings that absorbed sunlight energy, the time for ice to melt on the surface was recorded as the temperature increased. A 40 μL distilled water droplet was placed on the surface of the prepared free-standing films and cooled to subzero temperatures ($-10~^{\circ}\mathrm{C}$) in a cold chamber. During this process, the surface temperature was monitored using an IR camera, and ice melting was recorded with a high-speed camera at 2000 fps. Fig. 2 shows the schematic of the photothermal test setup.

The thermomagnetic properties of the samples were assessed at 28 \pm 2 °C and subzero temperatures (-10 ± 0.2 °C). A custom solenoid (height 530 mm, diameter 259 mm) generated the magnetic field. An alternating current (AC) with a frequency of 60 Hz was supplied to the coil, and the resulting magnetic field was measured with a Tesla meter (Model DX-160 Gauss).

To calculate the magnetic field produced by a current of 147 A, we applied the formula [39,40]

$$B = \frac{In\mu_0}{2} |\cos\alpha_2 - \cos\alpha_1|,\tag{1}$$

where μ_0 (the permeability of free space) is $4{\cdot}\pi\times 10^{-7}$ T·m/A, I is the

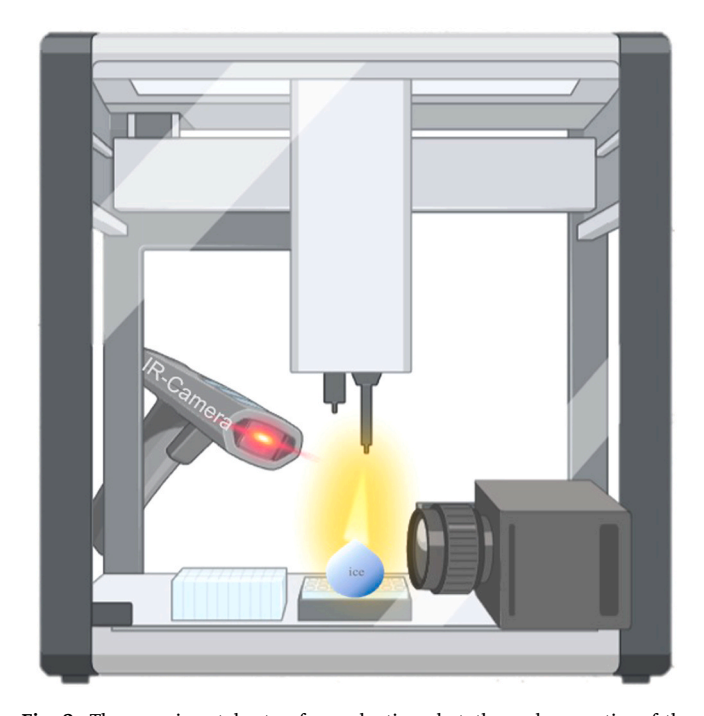


Fig. 2. The experimental setup for evaluating photothermal properties of the produced coatings.

current, and r is the distance from the upper side of the solenoid (15 cm), *n* is the number of coils per unit length (28 for this study), and α_1 and α_2 are the angles to position points 1 and 2 relative to the sample center $(60^{\circ}$ and 20° , respectively). The measured value of the magnetic field was 3.5 mT. To focus solely on the coatings' properties and eliminate any substrate effects, we conducted photothermal and thermomagnetic evaluations using freestanding films of the coating. An Optris PIX infrared camera tracked the surface temperature of the sample during the test to evaluate the de-icing process. A cylindrical plastic mold with a diameter of 1 cm was placed on the samples and then moved to a cold chamber at $-10.0~^{\circ}\text{C} \pm 0.2~^{\circ}\text{C}.$ The molds were filled with distilled water and left in the chamber for 24 h to create a frozen water column. The following day, the samples were positioned on the apparatus holder, and the temperatures of the ice and surface were monitored using an IR camera. The ice detachment process was recorded with a high-speed camera at 2000 fps. Fig. 3 shows a schematic of the magnetic-test setup.

3. Results and discussion

3.1. Surface characterization

To assess the wettability of the nanocomposite coatings, we first investigated the effect of varying the concentrations of Fe_3O_4 on the

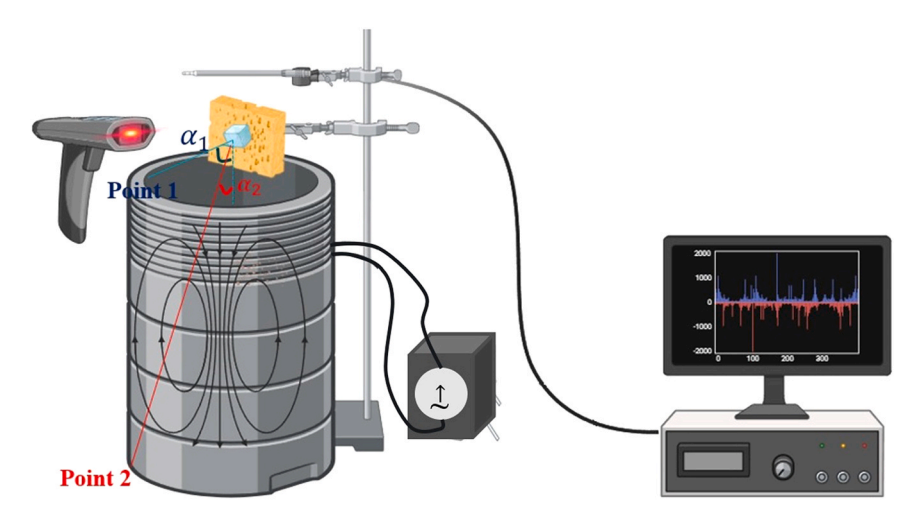


Fig. 3. The experimental setup for evaluating the thermomagnetic properties of the prepared coatings.

surface hydrophobicity. The CA of the SFe0 sample was 108.5° (Table 1). Adding 10, 20, and 30 wt% of oil-treated Fe₃O₄ increased the CA to 111.1° , 114.0° , and 116.2° , respectively. This increase in the CA may be due to the presence of oil-treated nanoparticles on the surface. However, the change was not significant, likely because of the similar surface chemistry of silicone oil and silicone resin [40]. In contrast, the SA was more affected by the nanoparticle concentration, decreasing from 33.2° for SFe0 to 12.1° for SFe20 and 10.8° for SFe30 (Table 1). This reduction occurs because of the slippery nature of silicone oil and the high concentration of nanoparticles, which affects surface slipperiness and eliminates pinning points [41].

Fig. 4 presents FE-SEM images of the hybrid coatings having Fe_3O_4 nanoparticle concentrations ranging from 10 wt% to 30 wt%. In Fig. 4a1 and a2, clear protuberances appear in the SFe10 and SFe20 coatings, whereas Fig. 4a3 shows agglomerated microclusters of nanoparticles in SFe30. The concentration of 30 wt% nanoparticles significantly alters the surface structure, leading to dominant nanoparticle aggregation. Fig. 4b displays FE-SEM elemental mapping of Fe_3O_4

Table 1 Wettability parameters of SFe0, SFe10, SFe20, and SFe30.

Sample code	Contact angle (°)	Contact angle hysteresis (°)	Sliding angle
SFe0	108.5 108.7	76.3 ± 2.1	33.2 ± 0.5
SFe10	± 0.2	44.8 ± 3.0	20.1 ± 1.3
SFe20	± 0.8	19.8 ± 1.3	12.1 ± 0.8
SFe30	± 0.7 ± 0.3 116.2 ± 0.3	18.1 ± 2.2	10.8 ± 1.2

nanocomposites, confirming the abundant presence of iron oxides and oxygen at the agglomerated sites, as well as carbon, silicon, oxygen, and iron throughout the coating. This agglomeration increased surface roughness (Fig. 5 and Table 2), where the mean height values of roughness increased with higher nanoparticle concentrations, reflecting a transition from smooth to textured surfaces. The SFe0 sample exhibited a relatively smooth structure (Fig. 5a), whereas nanoscale protrusions appeared in SFe10 and SFe20 (Fig. 5b, c), with SFe30 showing substantial agglomeration, resulting in nonuniform micronanocomposite roughness. This non uniformity in the SFe30 sample may likely affect the functional properties of the coatings, such as icephobicity [42].

In the three-dimensional height images from profilometry, the mean height values for SFe0, SFe10, SFe20, and SFe30 were 0.010, 0.042, 0.084, and 0.21 μm , respectively.

3.2. Anti-icing properties

The anti-icing performance of the hybrid coatings was evaluated by measuring their freezing delay and temperature. The temperature at which the water droplet began to freeze was recorded. Fig. 6 shows the effect of Fe₃O₄ concentration on the ice nucleation temperature of the hybrid coatings. The incorporation of Fe₃O₄ in the silicone coating lowered the ice nucleation temperature. The silicone coating's ice nucleation temperature dropped sharply from -17.4 °C for sample SF0 to $-25.1~^{\circ}\text{C}$ for sample SF20, whereas sample SFe30 showed only a 1 $^{\circ}\text{C}$ decrease relative to SFe20. The silicone oil on the surface of the nanoparticles enhances the anti-icing properties of silicone coatings by interacting with water droplets and reducing the number of ice nucleation sites [43]. This interaction delays surface icing, allowing the coating to maintain its icephobic qualities at low temperatures. The irregular trend and decrease in the ice nucleation temperature from SFe20 to SFe30 may be due to nanoparticle clusters and agglomeration, as discussed in Section 3.1. These agglomerations can create sites that are susceptible to ice formation [44]. Additionally, adding silicone oil-treated Fe₃O₄ to a silicone coating can delay the onset of ice formation [45]. The hydrophobic properties of silicone oil-treated Fe₃O₄ reduced the likelihood of water droplets adhering to the surface and freezing, effectively slowing ice accumulation. Thus, surface modification of nanoparticles with silicone oil creates conditions that are less favorable for ice nucleation and growth. The effect of silicone oiltreated Fe₃O₄ is evident in Fig. 6c, which shows that the freezing time for sample SFe20 was approximately 3548 s compared to 921 s for SFe0.

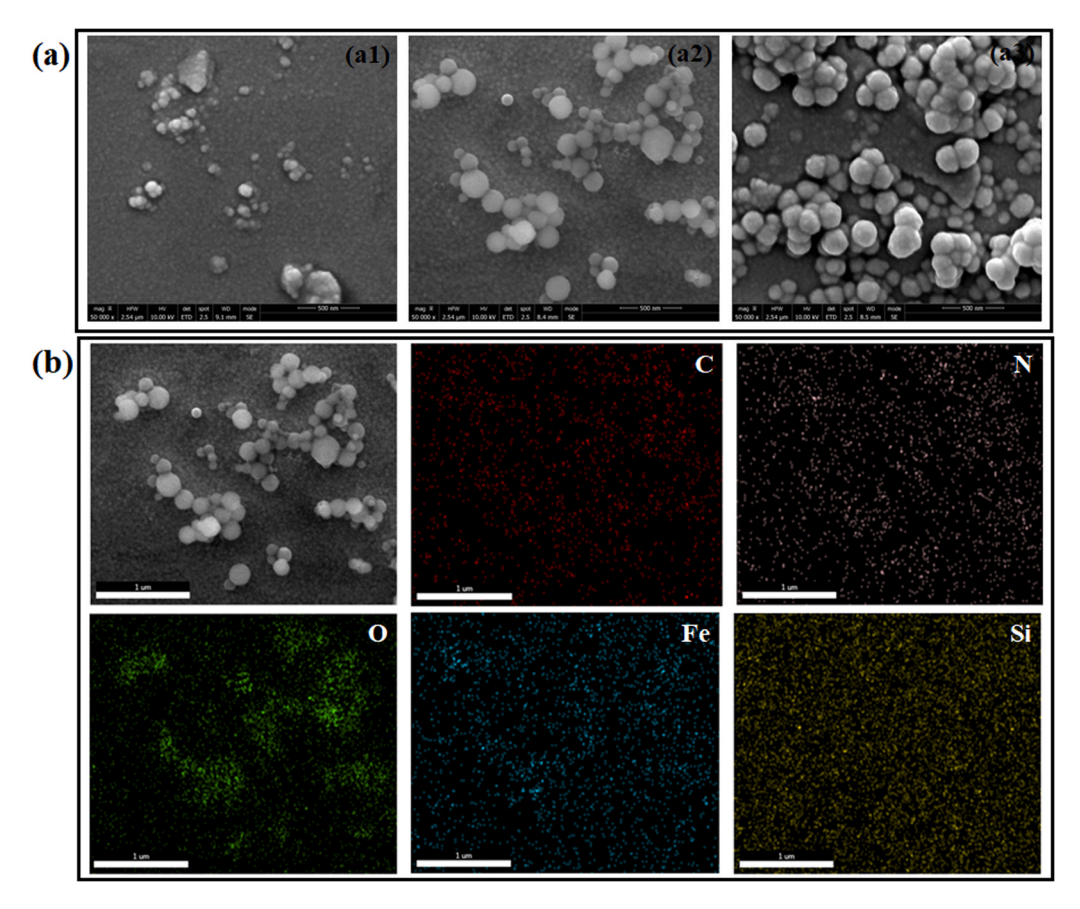


Fig. 4. Field emission scanning electron microscopy (FE-SEM) images of the surface structure of the coatings: (a1) SFe10, (a2) SFe20, (a3) SFe30, and (b) elemental distribution maps of SFe20 containing Fe, Si, C, O, and N.

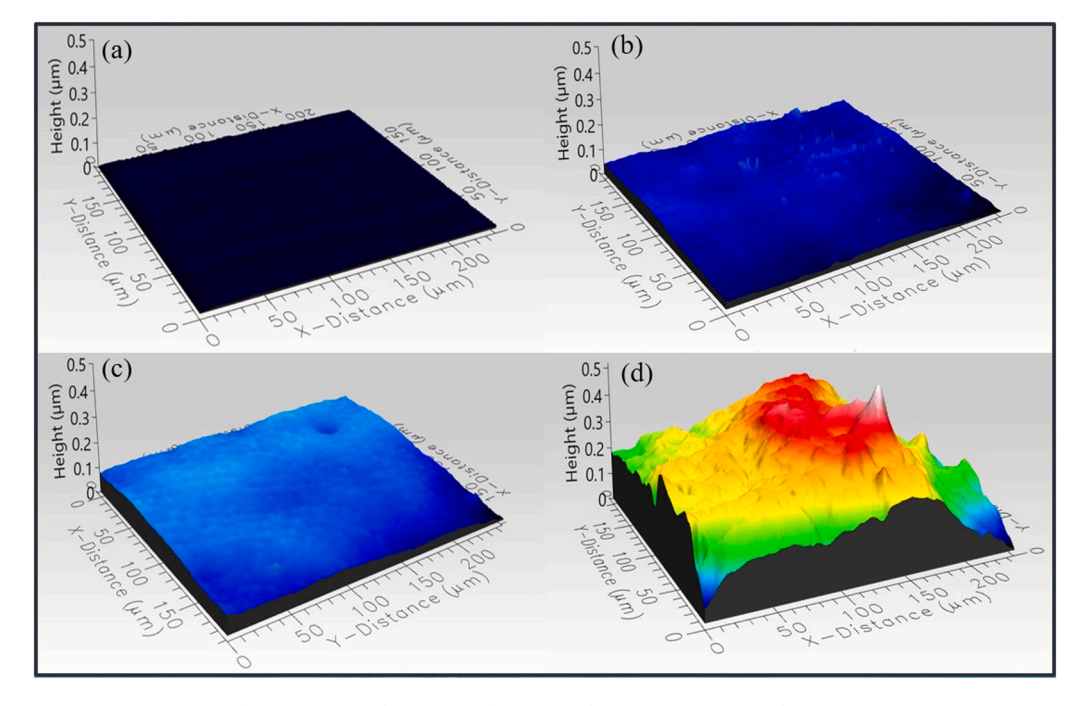


Fig. 5. Topography images of (a) SFe0, (b) SFe10, (c) SFe20, (d) SFe30.

3.3. Anti-icing/de-icing performance of the coatings

We using push-off tests to examine the effect of oil-treated iron oxide nanoparticles on the ice-adhesion strength of silicone-based coatings.

We found that incorporating nanoparticles into the polymer significantly reduced the ice-adhesion strength of the coatings. The average ice adhesion strength of the silicone-based coatings decreased from 156 to 46 kPa with the addition of Fe_3O_4 nanoparticles (Fig. 7a). The SFe20

Table 2
The mean roughness values of SFe0, SFe10, SFe20, and SFe30.

Sample code	Mean height (μm)	
SFe0	0.010 ± 0.001	
SFe10	0.042 ± 0.002	
SFe20	0.084 ± 0.001	
SFe30	0.21 ± 0.010	

coatings exhibited relatively lower ice adhesion strength because of changes in surface energy and interfacial interactions with ice. Oil treatment of Fe_3O_4 nanoparticles enhanced their hydrophobicity, altering the surface energy of the final coating and affecting the interaction with ice. The modified nanoparticles disrupt the hydrogen bonding network at the ice–coating interface, reducing ice adhesion strength [46]. Moreover, the presence of oil on the nanoparticles may cause slight surface restructuring under environmental conditions, further diminishing the ice-bonding capacity [46]. The increase in the ice adhesion strength of the SFe30 sample is linked to nanoparticle agglomeration, which increased the surface roughness and contact area

(Section 3.1), enhancing the mechanical interlocking with ice and leading to a higher adhesion strength [47]. These findings confirm the effectiveness of oil-treated $\rm Fe_3O_4$ nanoparticles at optimal concentrations for lowering freezing temperatures, delaying ice formation, and reducing ice adhesion strength.

The CA and SA of the surfaces were measured over 15 icing/de-icing cycles in a push-off test (Figs. 7b and 7c). CAs decreased by approximately 10° across all the samples. After 15 cycles, the SAs for SFe20 and SFe30 reached 13° and 16° , respectively, whereas the SA was 46° for SFe0. The low SA of the SFe20 sample indicated the presence of well-dispersed nanoparticles, which effectively reduced the ice-adhesion strength. Furthermore, the oil-treated nanoparticles on the surface of the coating reduced the pinned area of the water droplets and maintained this effect even after 15 cycles.

3.4. Photothermal characteristics thermal-induced melting behavior of the frozen droplet

The photothermal conversion efficiencies of the samples were evaluated by exposing them to simulated sunlight at 28 ± 2 °C. Before evaluation, the samples were placed on a 3 cm thick cubic foam to

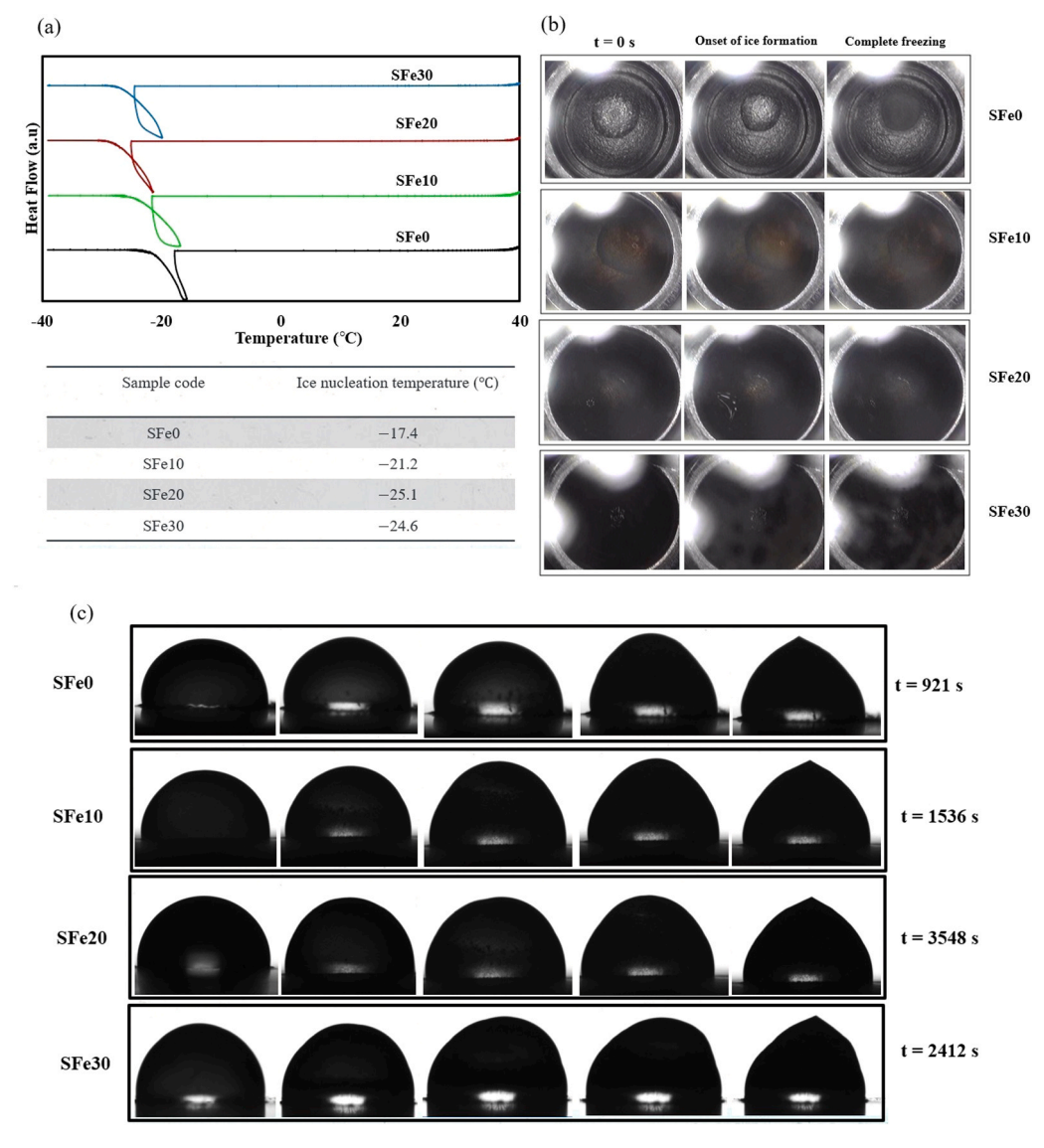


Fig. 6. Anti-icing properties of coatings; (a) evaluation by differential scanning calorimetry (DSC) of ice nucleation temperatures; (b) optical images of a top-down view of DSC aluminum pans during the cooling process; (c) time until ice formation on the surface of the SFe0, SFe10, SFe20, and SFe30 coatings and images of the corresponding shapes of the frozen droplets.

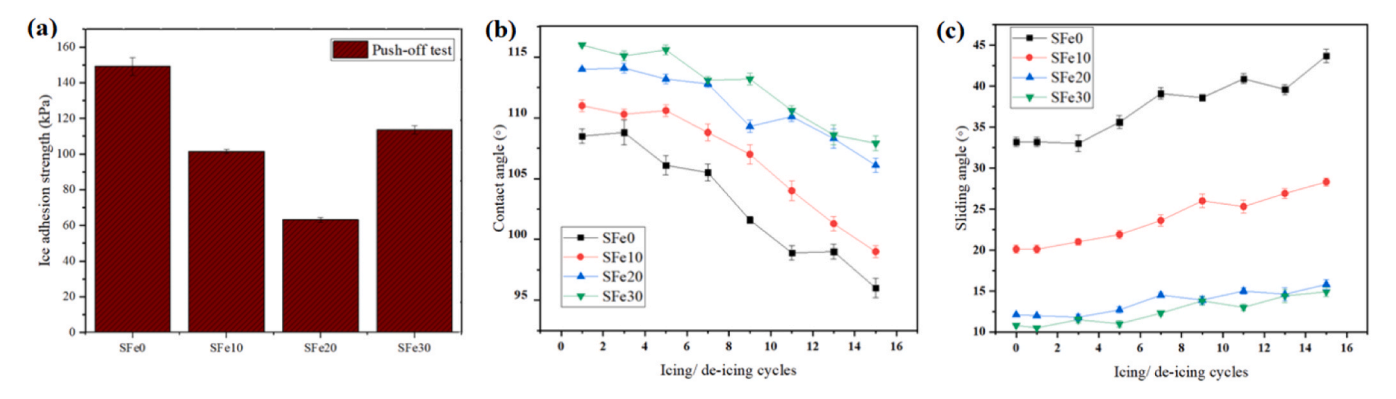


Fig. 7. (a) Ice adhesion strength measurements by push-off tests on the SFe0, SFe10, SFe20, and SFe30 coatings; (b) contact angles and (c) sliding angles of the SFe0, SFe10, SFe20, and SFe30 coatings over 15 icing/de-icing cycles.

minimize heat dissipation. After 210 s, the temperature of the SFe0 sample stabilized at approximately 44 °C, whereas those of the SFe10, SFe20, and SFe30 samples stabilized at 62, 88, and 89 °C, respectively (Fig. 8a). This result highlights the excellent photothermal conversion properties of SFe20 and SFe30. Because SFe20 exhibited a lower ice adhesion strength than the other samples and there was no significant difference between SFe20 and SFe30, we chose SFe20 to investigate the performance over multiple cycles. The SFe20 sample with 20 wt% of Fe₃O₄ nanoparticles, demonstrated excellent recyclability for photothermal activity, with almost no decline in reactivity after four cycles and negligible reduction in the fifth cycle (Fig. 8b). Each cycle exhibited

a similar temperature variation, which is crucial for the practical application of the coating [48].

We then assessed the effect of nanoparticle concentration on the deicing performance of the samples. The melting of ice droplets on the surfaces of the three samples began at the ice-coating interface (Fig. 8c). Sunlight radiating from above and at a constant room temperature of $-10\,^{\circ}\text{C}$ led to increased surface temperatures because of the heat generated by the samples. Fig. 8c illustrates that the ice–water boundary on the SFe10 sample was nonuniform, likely because of a nonuniform dispersal or insufficient quantities of nanoparticles in the coating, and the ice melted completely after 420 s. In contrast, the ice tip of the SFe20

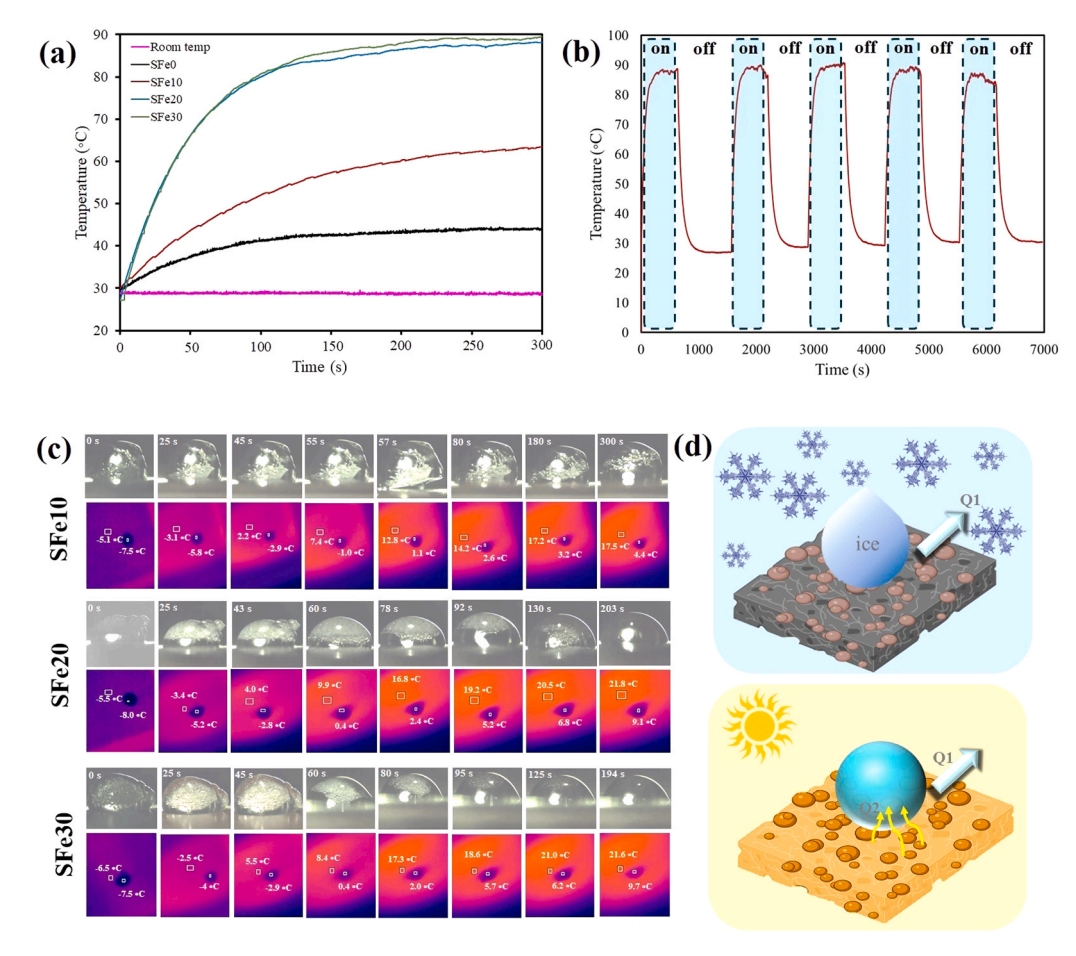


Fig. 8. (a) Surface temperatures of the SFe0, SFe10, SFe20, and SFe30 coatings under simulated illumination; (b) temperature variation of the SFe20 coating surface over repeated heating—cooling cycles; (c) optical and infrared thermal images of the SFe0, SFe10, SFe20, and SFe30 coatings during photothermal de-icing processes; (d) Schematic summarizing the photothermal activity of the coatings containing Fe_3O_4 nanoparticles.

sample disappeared within 60 s of sunlight exposure, with the ice-water boundary forming at the base in 45 s and then moving upward, resulting in the complete melting of the ice droplet in 203 s. The melting process of SFe30 is similar to that of SFe20. Infrared images during the de-icing process indicated that heat generation raised the samples' surface temperatures, with ice droplets melting completely when the temperature reached 21 °C. Moreover, the uniform distribution of heat on the SFe20 surface suggests the relatively even distribution of Fe₃O₄ particles throughout the coating [49]. The anti-icing mechanism is illustrated in Fig. 8d, where the thermal energy of the water droplet is denoted as Q1, and the heat produced by the coating under light exposure is denoted as Q2. In cold and dark environments, droplets tend to stick to the coating surface, making their removal difficult. During this time, heat (Q1) within the droplets diffuses into the colder surroundings, causing them to freeze. However, when exposed to light, the Fe₃O₄ nanoparticles generate significant heat (Q2), which is transferred from the coating surface into the frozen droplets, facilitating active de-icing [50].

In conclusion, SFe20 and SFe30 exhibited better de-icing

performances than the SFe10 coating.

3.5. Magnetic property and magnetothermal effect

To study the thermomagnetic properties of the hybrid coatings, we examined the effects of various Fe_3O_4 concentrations under an applied magnetic field at room temperature. The temperature increase correlated with the Fe_3O_4 concentration; for samples containing 10, 20, and 30 wt% Fe_3O_4 , the temperature increased by approximately 7.5, 9, and $10\,^{\circ}$ C, respectively, over $1000\,$ s at $147\,$ A and $3.5\,$ mT (Fig. 9a). To clarify the role of Fe_3O_4 nanoparticles in enhancing the thermomagnetic behavior, we analyzed the temperature change (ΔT) of samples with and without Fe_3O_4 under a magnetic field. ΔT consistently increased over time for all samples, with Fe_3O_4 nanoparticles significantly enhancing the magnetic thermal effect. Specifically, the surface temperatures of the samples containing 20 and 30 wt% Fe_3O_4 were 29 and 30.3 °C, respectively. The observed ΔT was comparable to that reported by Zhang et al [51]. When magnetic coatings are exposed to a

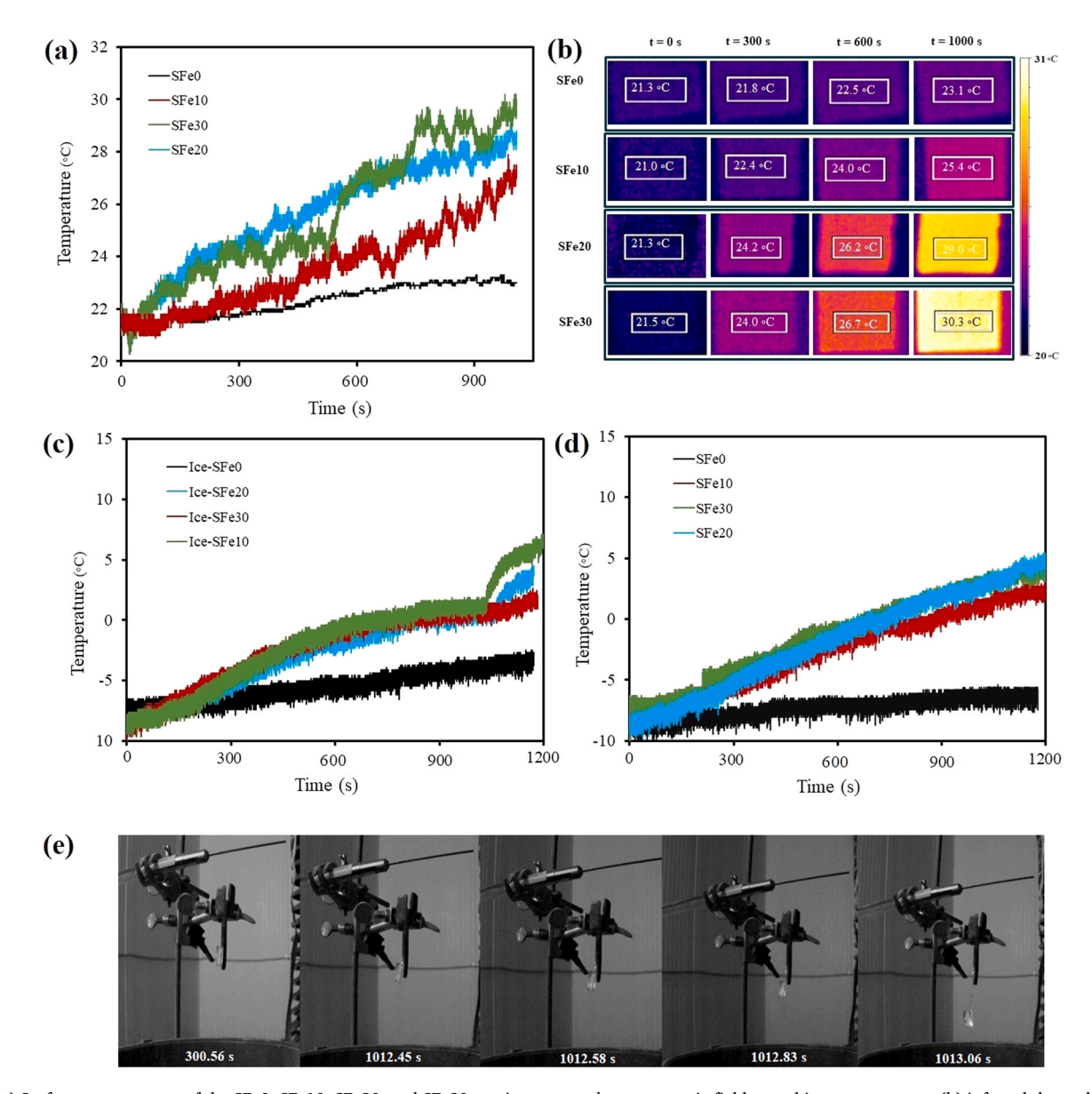


Fig. 9. (a) Surface temperatures of the SFe0, SFe10, SFe20, and SFe30 coatings exposed to a magnetic field at ambient temperature; (b) infrared thermal images of the SFe0, SFe10, SFe20, and SFe30 coatings during a magnetic test at ambient temperature; (c) temperature variations of the ice-covered SFe0, SFe10, SFe20, and SFe30 coatings exposed to the magnetic field at -10 °C, (d) temperature variations of the ice-covered SFe0, SFe10, SFe20, and SFe30 coatings exposed to the magnetic field at -10 °C; (e) optical images of de-icing process during the magnetic test at -10 °C.

high-frequency magnetic field, the heat generation in magnetic nanoparticles is controlled by Néel relaxation, Brownian relaxation, and hysteresis loss mechanisms [52]. Additionally, this heat generation occurs in magnetic fields exceeding 1 mT, and increasing the field strength and nanoparticle concentration directly affects heating efficacy [52,53]. Infrared imagery of the samples over time (Fig. 9b) confirmed that the heat generation within the nanocomposite increased the surface temperature, which was evenly distributed.

To examine the de-icing capabilities in relation to thermomagnetic properties, we formed cylindrical ice forms on the surface using silicone molds and subjected them to a magnetic field of 3.5 mT. Fig. 9c, d shows the temperature/time diagrams for samples with an ice mold on the surface and the area outside the ice placement zone, respectively. When the ice began to melt (Fig. 9c), the temperature clearly demonstrated a phase transition from solid to liquid, resulting in a nonlinear pattern after 5 min of exposure to the magnetic field; a linear behavior was observed where the ice was absent (Fig. 9d). Fig. 9e shows an optical image of the de-icing process during the magnetic test at -10 °C. When the ice detached from the surface, the surface temperature increased immediately. The magnetic field influenced the water molecules within the ice, inducing oscillations that increased their kinetic energy, raised the temperature, and ultimately melted the ice by disrupting hydrogen bonds between water molecules [54]. In contrast, when no ice was present on the surface, the temperature increased continuously in a linear manner, with heat generation causing an increase of approximately 15 °C over 20 min for the SFe20 sample, which was approximately 12 °C higher than that of the sample without Fe₃O₄. Although this ΔT was comparable with that reported in the literature [51,53], transmission lines operating in a higher current range (300-3800 A) and power (12-3000 MW) create a stronger magnetic field around the coating. Studies on a 400 kV T-Pylon observed that magnetic field intensities varied from 13.83 mT at 1 cm from the surface to 6.05 mT at 10 cm and further decreased to 0.6 mT at 1 m. For context, the typical magnetic field strength 1 m above the ground beneath such a pylon generally ranges from 5 to 10 μ T, with peak values reaching up to 100 μ T [55–58]. These data suggest that the surface temperatures of the magnetic coatings could exceed the levels obtained under laboratory conditions.

3.6. Mechanistic insight into photothermal and magnetothermal anti-Icing with silicone-oil-modified Fe_3O_4 nanoparticles

The enhanced anti-icing performance of the SFe20 coating stems from a well-orchestrated interplay between photothermal and magnetothermal heating effects, both activated by the presence of Fe $_3$ O4 nanoparticles, and amplified through their surface functionalization with silicone oil. These effects are synergistically coupled with interfacial wetting modifications, enabling effective and energy-efficient ice melting under various environmental stimuli (Fig.10).

Under solar illumination, the Fe₃O₄ nanoparticles embedded in the silicone matrix act as efficient photothermal agents by absorbing visible and near-infrared light. The absorbed photons are converted into heat via non-radiative relaxation pathways, which raise the local surface temperature and promote rapid melting of ice at the coating ice interface. This photothermal response is enhanced by the uniform distribution of nanoparticles facilitated by silicone oil modification, ensuring homogenous heat release across the surface. The heat (Q2) generated offsets the thermal energy (Q_1) loss from the droplet to the environment, thus delaying freezing and promoting melting (see Fig. 8d). Notably, the SFe20 sample exhibited a surface temperature rise from -5 °C to over 21 °C under simulated sunlight (1 kW/m²), melting ice droplets in less than 210 s. These results are consistent with the findings of Xue et al. and Xiao et al., who reported significant temperature increases in Fe₃O₄based coatings under similar photonic exposure, enabling rapid frost removal on polymer substrates [35,59].

Beyond photothermal effects, the nanocomposite system leverages magnetothermal heating when exposed to an alternating magnetic field. Fe₃O₄ nanoparticles possess superparamagnetic characteristics at the nanoscale, which under AC magnetic excitation (3.5 mT), lead to heat generation through both Néel and Brownian relaxation processes. Néel relaxation arises from internal rotation of the magnetic moments against anisotropy barriers, while Brownian relaxation reflects physical rotation of the particles within the polymer matrix. Although the chance of Brownian relaxation is negligible, both mechanisms dissipate energy as heat. In the SFe2O sample, this magnetothermal activation caused a surface temperature increase of over 15 °C and melting the ice by disrupting hydrogen bonds [46,60].

Importantly, the surface modification of Fe₃O₄ with silicone oil played a decisive role not only in nanoparticle dispersion but also in tuning the interfacial energy landscape. Silicone oil imparts a slippery,

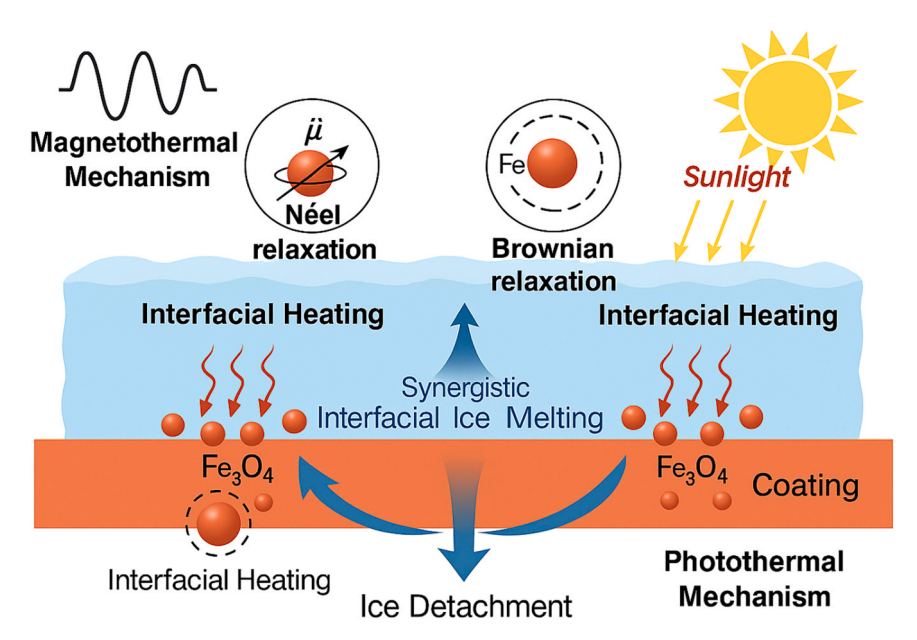


Fig. 10. Schematic illustration of mechanistic insight into photothermal and magnetothermal anti-Icing with silicone-oil-modified Fe₃O₄ nanoparticles.

low-energy surface, suppressing ice nucleation by reducing heterogeneous nucleation sites. This multifunctional role of silicone oil is well supported by previous literature [41]. In our system, these modifications resulted in a dramatic reduction of sliding angle (SA) from 33° (SFe0) to 12° (SFe20) and extended freezing delay time from 921 s to 3548 s.

Unlike purely passive coatings, the dual-responsive SFe20 can activate heating either by natural sunlight or electromagnetic fields typical around power lines. Considering the electromagnetic environment of high-voltage lines, such coatings can passively harness ambient fields for self-heating, thus reducing ice-related risks without external intervention.

In summary, the nanocomposite coating achieves a functional synergy between photothermal and magnetothermal mechanisms, optimized through nanoscale engineering of surface chemistry. This approach overcomes the limitations of conventional coatings that rely solely on passive wetting properties or active Joule heating. The SFe20 system demonstrates that by tailoring both material composition and energy transduction pathways, high-performance anti-icing behavior can be achieved with operational simplicity, durability, and minimal energy input critical factors for sustainable infrastructure protection in cold. Fig. 10

4. Conclusion

This study confirms the effectiveness of silicone-based coatings infused with Fe₃O₄ nanoparticles for the de-icing of power transmission lines. Nanocomposite coatings use their thermomagnetic and photothermal properties to convert magnetic and solar energy into heat, thereby facilitating efficient ice melting. The physicochemical properties of the coatings were analyzed using CA and SA measurements, FE-SEM, and profilometry. We found that increasing the Fe₃O₄ concentration enhanced surface hydrophobicity and roughness. The static CA of water on the SFe20 sample was 114°, with a SA of 12°, demonstrating the positive effect of incorporating 20 wt% nanoparticles on the coating's icephobic properties. Additionally, surface roughness data indicated that higher nanoparticle concentrations increased roughness from 0.01 to 0.2 µm, likely through nanoparticle aggregation. The coatings containing 20 wt% Fe₃O₄ nanoparticles improved icephobic properties, significantly reducing ice adhesion from 156 to 46 kPa and extending nucleation time from 921 to 3548 s, crucial for maintaining power infrastructure integrity in cold climates. Our evaluation of photothermal and thermomagnetic properties showed that the SFe20 sample was highly sensitive to sunlight, generating heat even under lowtemperature conditions and increasing the temperature from -5 to 21 °C, which caused ice to melt within 203 s. The thermomagnetic behavior of the SFe20 sample also melted the ice mold and raised the surface temperature from -10 to 5 °C.

Overall, this innovative coating strategy offers a promising, energyefficient solution for mitigating ice-related failures in the power industry, with the potential to reduce operational costs and enhance sustainability in harsh winter environments.

CRediT authorship contribution statement

Shamim Roshan: Writing – original draft, Visualization, Validation, Software, Methodology, Investigation, Data curation. Gelareh Momen: Writing – review & editing, Validation, Supervision, Project administration. Issouf Fofana: Writing – review & editing, Validation, Data curation. Reza Jafari: Writing – review & editing, Validation, Supervision, Methodology, Data curation, Conceptualization. Stephan Brettschneider: Writing – review & editing, Visualization, Validation, Methodology, Data curation, Conceptualization.

Declaration of Competing Interest

The authors declare that they have no known competing financial

interests or personal relationships that could have appeared to influence the work reported in this paper.

Acknowledgment

The authors wish to acknowledge the financial support provided by the Natural Sciences and Engineering Research Council of Canada, NSERC (RGPIN: 2023-05279), the Université du Québec à Chicoutimi (UQAC), and the Research Centre for High Performance Polymer and Composite Systems (CREPEC). Additionally, the authors extend their gratitude to Luc Chatigny for his technical work and assistance with the magnetic tests.

Data availability

Data will be made available on request.

References

- W. Henson, R. Stewart, B. Kochtubajda, On the precipitation and related features of the 1998 ice storm in the Montréal area, Atmos. Res. 83 (1) (2007) 36–54.
- [2] H.M. Merrill, J.W. Feltes, Transmission icing: a physical risk with a physical hedge. 2006 IEEE Power Engineering Society General Meeting, IEEE, 2006, June, p. 7.
- [3] S.G. Moghadam, G. Momen, E. Bakhshandeh, R. Jafari, To be or not to be a hydrophobic matrix? The role of coating hydrophobicity on anti-icing behavior and ions mobility of ionic liquids, Chem. Eng. J. 485 (2024) 149696.
- [4] M. Farzaneh (Ed.), Atmospheric Icing of Power Networks, Springer Science & Business Media. 2008.
- [5] H. Mc Innes, J.E. Haugen, J.E. Kristjánsson, B.E.K. Nygaard, R. Rasmussen, S. Solberg, K. Blennow, O.E. Tveito, Wind ice and snow load impacts on infrastructure and the natural environment (WISLINE). Proceedings of the 19th EGU General Assembly, Vienna, Austria, 2017, pp. 23–28.
- [6] S. Heydarian, G. Momen, R. Jafari, Icephobicity and electrical assessment of slippery coating impregnated with a stabilized hydroxyl-terminated lubricant for high voltage insulation application, J. Mater. Sci. 58 (22) (2023) 9264–9281.
- [7] M. Farzaneh, F. Jakl, Coatings for protecting overhead power network equipment in winter conditions: working group B2. 44, Cigré, 2015.
- [8] A.R. Solangi, Icing effects on power lines and anti-icing and de-icing methods (Master's thesis), UiT, The Arctic University of Norway, 2018.
- [9] M.A. Saffar, A. Eshaghi, M.R. Dehnavi, Fabrication of superhydrophobic, selfcleaning and anti-icing ZnO/PTFE-SiO₂ nano-composite thin film, Mater. Chem. Phys. 259 (2021) 124085.
- [10] Y. Wu, X. Li, C. Mi, L. Zong, X. Wang, Preparation and characterization of perfluorine-SiO₂ nanoparticles and superhydrophobic fluorosilicone/silica hybrid composite coating, Appl. Phys. A Mater. Sci. Process. 125 (4) (2019) 250.
- [11] J. Lv, Y. Song, L. Jiang, J. Wang, Bio-inspired strategies for anti-icing, ACS Nano 8 (4) (2014) 3152–3169.
- [12] M. Farzaneh, W.A. Chisholm, Systems for de-icing overhead power line conductors and ground wires. Techniques for Protecting Overhead Lines in Winter Conditions: Dimensioning, Icephobic Surfaces, De-Icing Strategies, Springer International Publishing, Cham, 2022, pp. 157–194.
- [13] H. Chen, F. Wang, H. Fan, R. Hong, W. Li, Construction of MOF-based superhydrophobic composite coating with excellent abrasion resistance and durability for self-cleaning, corrosion resistance, anti-icing, and loading-increasing research, Chem. Eng. J. 408 (2021) 127343.
- [14] C. Zhang, Y. Lei, K. Wang, B. Jiang, G. Ye, Y. Yuan, K. Sun, Q. Chen, T. Liu, Durable fluorine-free multilayer superhydrophobic coatings for synergistic photothermal and electrothermal anti-icing protection, Prog. Org. Coat. 208 (2025) 109433.
- [15] Z. Gao, T. Xu, X. Miao, J. Lu, X. Zhu, Y. Song, G. Ren, Y. Jia, X. Li, A thermal-driven self-replenishing slippery coating, Surf. Interfaces 24 (2021) 101022.
- [16] T.B. Nguyen, S. Park, Y. Jung, H. Lim, Effects of hydrophobicity and lubricant characteristics on anti-icing performance of slippery lubricant-infused porous surfaces, J. Ind. Eng. Chem. 69 (2019) 99–105.
- [17] M.I. Jamil, Q. Wang, A. Ali, M. Hussain, T. Aziz, X. Zhan, Q. Zhang, Slippery photothermal trap for outstanding deicing surfaces, J. Bionic Eng. 18 (2021) 548–558.
- [18] S. Wu, Y. Du, Y. Alsaid, D. Wu, M. Hua, Y. Yan, B. Yao, Y. Ma, X. Zhu, X. He, Superhydrophobic photothermal icephobic surfaces based on candle soot, Proc. Natl. Acad. Sci. USA 117 (21) (2020) 11240–11246.
- [19] X. Liu, H. Chen, Z. Zhao, Y. Yan, D. Zhang, Slippery liquid-infused porous electric heating coating for anti-icing and de-icing applications, Surf. Coat. Technol. 374 (2019) 889–896.
- [20] J. Huang, D. Li, Z. Peng, B. Zhang, Y. Yao, S. Chen, High-efficient anti-icing/ deicing method based on graphene foams, ACS Appl. Mater. Interfaces 15 (36) (2023) 43026–43037.
- [21] J. Huang, Z. Peng, B. Zhang, Y. Yao, S. Chen, A flexible and high-efficient antiicing/deicing coating based on carbon nanomaterials, ACS Appl. Mater. Interfaces 16 (33) (2024) 44210–44224.

- [22] Working Group B2.69, CIGRÉ; Santos Yubero, Héctor de, Coatings for protecting overhead power networks against icing, corona noise, corrosion and reducing their visual impact. CIGRÉ Technical Brochure 838. (CIGRE (Paris, Francia), 01/06/2021).
- [23] D. Shi, M.E. Sadat, A.W. Dunn, D.B. Mast, Photo-fluorescent and magnetic properties of iron oxide nanoparticles for biomedical applications, Nanoscale 7 (18) (2015) 8209–8232.
- [24] Y. Sood, H. Mudila, P. Chamoli, P. Saini, A. Kumar, Exploring the efficacy and future potential of polypyrrole/metal oxide nanocomposites for electromagnetic interference shielding; a review, Mater. Horiz. 11 (2024) 4256–4274.
- [25] H. Gao, Y. Zhou, J. Ma, H. Jin, J. Bao, D. Wen, Recent advancements in electrothermal anti-/de-icing materials, RSC Adv. 15 (22) (2025) 17102–17115.
- [26] E.M. Materón, C.M. Miyazaki, O. Carr, N. Joshi, P.H. Picciani, C.J. Dalmaschio, F. Davis, F.M. Shimizu, Magnetic nanoparticles in biomedical applications: a review, Appl. Surf. Sci. Adv. 6 (2021) 100163.
- [27] J. Tang, M. Myers, K.A. Bosnick, L.E. Brus, Magnetite Fe₃O₄ nanocrystals: spectroscopic observation of aqueous oxidation kinetics, J. Phys. Chem. B 107 (30) (2003) 7501–7506.
- [28] M.Y. Razzaq, M. Behl, A. Lendlein, Memory-effects of magnetic nanocomposites, Nanoscale 4 (20) (2012) 6181–6195.
- [29] C.C. Hsu, C.S. Wu, Y.L. Liu, Multiple stimuli-responsive poly (vinylidene fluoride) (PVDF) membrane exhibiting high efficiency of membrane clean in protein separation, J. Membr. Sci. 450 (2014) 257–264.
- [30] P. Calcagnile, D. Fragouli, I.S. Bayer, G.C. Anyfantis, L. Martiradonna, P.D. Cozzoli, R. Cingolani, A. Athanassiou, Magnetically driven floating foams for the removal of oil contaminants from water, ACS Nano 6 (6) (2012) 5413–5419.
- [31] Y. Xu, J. Yuan, B. Fang, M. Drechsler, M. Müllner, S. Bolisetty, M. Ballauff, A. H. Müller, Hybrids of magnetic nanoparticles with double-hydrophilic core/shell cylindrical polymer brushes and their alignment in a magnetic field, Adv. Funct. Mater. 20 (23) (2010) 4182–4189.
- [32] L.G.D. Santos, D.D.A. Buelvas, D.F. Valezi, B.L.S. Vicentin, C.M.M. Rocha, E. D. Mauro, F. d A.L. Porta, Microstructural and magnetic properties of polyamide-based recycled composites with iron oxide nanoparticles, Magnetism 5 (1) (2025)
- [33] F. Edmir, N.B. Kilic, S. Bilici, O. Karakaya, F.E. Baskara, H.A. Reis, Fe₃O₄/expanded graphite/paraffin nanocomposites for both electromagnetic interference shielding and heat management, Mater. Chem. Phys. 332 (2025) 130277.
- [34] A.P. Singh, M. Mishra, S.K. Dhawan, Conducting multiphase magnetic nanocomposites for microwave shielding application, Nanomagnetism 2 (2015) 246–277.
- [35] Y. Xue, Y. Wang, Y. Wang, X. Sui, W. Liang, F. Wang, A superhydrophobic Fe₃O₄/PEI nanocomposite film with active activation function for anti-icing/deicing applications, Mater. Today Sustain. 24 (2023) 100588.
- [36] G. Zhang, Q. Zhang, T. Cheng, X. Zhan, F. Chen, Polyols-infused slippery surfaces based on magnetic Fe₃O₄-functionalized polymer hybrids for enhanced multifunctional anti-icing and deicing properties, Langmuir 34 (13) (2018) 4052–4058.
- [37] X. Xiao, X. Wei, J. Wei, J. Wang, Multifunctional Fe3O4-based photothermal superhydrophobic composite coating for efficient anti-icing/deicing, Sol. Energy Mater. Sol. Cells 256 (2023) 112313.
- [38] T. Cheng, R. He, Q. Zhang, X. Zhan, F. Chen, Magnetic particle-based superhydrophobic coatings with excellent anti-icing and thermoresponsive deicing performance, J. Mater. Chem. A Mater. Energy Sustain. 3 (43) (2015) 21637–21646
- [39] N. Seifaddini, B. Sekongo, I. Fofana, S. Akre, A. Chehri, M. Ouhrouche, Towards winding deformation assessment from vibration signals using an optical sensor, IET Sci. Meas. Technol. 19 (1) (2025) e12224.
- [40] M. Seguin, Physics XXI volume B: electricity and magnetism, EPRI, 2022.
- [41] W. Cui, T.A. Pakkanen, Icephobic performance of one-step silicone-oil-infused slippery coatings: effects of surface energy, oil and nanoparticle contents, J. Colloid Interface Sci. 558 (2020) 251–258.

- [42] P. Zhang, C. Wu, L. Xie, B. Xue, Y. Jiang, Superhydrophobic photothermal coating comprising SiO₂-grafted Fe₃O₄ and ag decorated reduced graphene for anti-icing and de-icing, Surf. Coat. Technol. 489 (2024) 131127.
- [43] Y. Du, J. Tang, R. Li, J. Liu, R. Chen, J. Yu, P. Liu, J. Wang, A crosslinked silicone coating adjusted by an additive with promising antifouling and ice nucleation inhibition performance, N. J. Chem. 48 (2) (2024) 693–702.
- [44] S. Heydarian, R. Jafari, G. Momen, Icephobic behavior of a slippery coating containing nanoporous particles as lubricant-loaded carriers, Surf. Interfaces 41 (2023) 103306.
- [45] S. Roshan, A.A. Sarabi, R. Jafari, G. Momen, One-step fabrication of superhydrophobic nanocomposite with superior anticorrosion performance, Prog. Org. Coat. 169 (2022) 106918.
- [46] G.C. Hermosa, L.H. Fang, C.S. Liao, C.F. Chang, Y.L. Chiu, C.H. Chang, S.F. Wang, A.A.C. Sun, Application of oleic acid functionalized Fe₃O₄ magnetic nanoparticles for adsorption of oil from emulsified solutions. 2023 IEEE International Magnetic Conference-Short Papers (INTERMAG Short Papers), IEEE, 2023, May, pp. 1–2.
- [47] X. Wu, Z. Chen, A mechanically robust transparent coating for anti-icing and selfcleaning applications, J. Mater. Chem. A Mater. Energy Sustain. 6 (33) (2018) 16043–16052.
- [48] S. Heydarian, G. Momen, R. Jafari, Icephobicity and electrical assessment of slippery coating impregnated with a stabilized hydroxyl-terminated lubricant for high voltage insulation application, J. Mater. Sci. 58 (22) (2023) 9264–9281.
- [49] C. Chen, Z. Tian, X. Luo, G. Jiang, X. Hu, L. Wang, R. Peng, H. Zhang, M. Zhong, Cauliflower-like micro-nano structured superhydrophobic surfaces for durable anti-icing and photothermal de-icing, Chem. Eng. J. 450 (2022) 137936.
- [50] Y.H. Lei, G.J. Ye, B.C. Jiang, L. Wen, X.C. Mo, X.J. Lei, Y.L. Zhang, Y. Yuan, X. T. Chang, Ice-resistant Fe₃O₄@ PPy coating: enhancing stability and durability with photothermal super hydrophobicity, Prog. Org. Coat. 196 (2024) 108704.
- [51] W. Zhang, X. Liang, C. Li, F. Li, L. Zhang, H. Yang, Optical and thermal properties of Fe₃O₄ nanoparticle-doped cholesteric liquid crystals, Liq. Cryst. 45 (8) (2018) 1111–1117
- [52] R.R. Shah, T.P. Davis, A.L. Glover, D.E. Nikles, C.S. Brazel, Impact of magnetic field parameters and iron oxide nanoparticle properties on heat generation for use in magnetic hyperthermia, J. Magn. Magn. Mater. 387 (2015) 96–106.
- [53] O.M. Lemine, S. Algessair, N. Madkhali, B. Al-Najar, K. El-Boubbou, Assessing the heat generation and self-heating mechanism of superparamagnetic Fe₃O₄ nanoparticles for magnetic hyperthermia application: the effects of concentration, frequency, and magnetic field, Nanomaterials 13 (3) (2023) 453.
- [54] I.V. Kudryakov, V.S. Efimchenko, G.G. Fetisov, M.A. Korotkova, A.R. Oganov, High-density ice ih obtained by crystallization of water in a high-frequency electromagnetic field, Crystals 13 (5) (2023) 821.
- [55] M.G. Unde, B.E. Kushare, Analysis of electromagnetic fields of 1200kV UHV-AC transmission lines. 2013 5th International Conference and Computational Intelligence and Communication Networks, IEEE, 2013, September, pp. 580–584.
- [56] S.A. Saleem, M. Mihoub, H.A. Al Hatmi, M.I. Al Zarouni, Evaluation of electromagnetic field intensity of EHV transmission lines and substations at two extremely different climatic conditions in Oman. 2024 International Conference on Futuristic Technologies in Control Systems & Renewable Energy (ICFCR), IEEE, 2024, September, pp. 1–6.
- [57] H. Zhou, W. Qiu, K. Sun, J. Chen, X. Deng, F. Qian, D. Wang, B. Zhao, J. Li, S. Li, Y. Qiu (Eds.), Ultra-high voltage AC/DC power transmission, Springer, Berlin, Germany, 2018, pp. 857–868.
- [58] S. Shepherd, M.A.P. Lima, E.E. Oliveira, S.M. Sharkh, C.W. Jackson, P.L. Newland, Extremely low frequency electromagnetic fields impair the cognitive and motor abilities of honey bees, Sci. Rep. 8 (1) (2018) 7932.
- [59] T. Xiao, S. Tu, S. Liang, R. Guo, T. Tian, P. Müller-Buschbaum, Solar cell-based hybrid energy harvesters towards sustainability, OptoElectron. Sci. 2 (6) (2023) 230011. -230011.
- [60] I.A. Shah, G. Xu, N. ul Hassan, M. Arif, Y. You, J. Liu, Y. Gong, X. Miao, F. Xu, Structural and magneto-transport properties of Mn1+ xCo1- xsn (x= 0.0-1.0) alloys, J. Magn. Magn. Mater. 465 (2018) 360-364.